PCCP

ROYAL SOCIETY OF CHEMISTRY

PAPER

View Article Online
View Journal

Cite this: DOI: 10.1039/d5cp03997e

The superior catalytic effect of N *vs.* Ni for improving hydrogen storage kinetics of $LiBH_4$@X-doped-C-MSU-H (X = N or Ni) nanoporous carbon composites

Petru Palade, * Catalin Negrila, Anca G. Mirea, Cristian Radu and Cezar Comanescu

Lithium borohydride ($LiBH_4$) is a promising hydrogen storage material releasing 13.8 wt% H_2 upon decomposition in lithium hydride and boron, significantly surpassing other complex hydrides. However, sluggish dehydrogenation kinetics still hinder the use for practical applications. The infiltration of $LiBH_4$ into carbon nanoscaffolds has proved to be effective in improving the hydrogen absorption/desorption (a/d) kinetics. Further improvement of storage kinetics can be achieved by modification of the nanocarbon with dopant elements. The present work compares nanoporous carbon (C-MSU-H) and C-MSU-H doped either with 1 at% N or 1 at% Ni as the matrix for infiltration of $LiBH_4$. The catalytic effect of nitrogen proved to be superior to that of nickel (keeping the same doping level) for improving the hydrogen a/d kinetics of $LiBH_4$ infiltrated in doped C-MSU-H. X-ray photoelectron spectroscopy was used to detect the amount and chemical proximity of nitrogen in nanoporous carbon following the thermal treatment in ammonia flow. The morphology and porosity of doped C-MSU-H were investigated by X-ray diffraction, FTIR, TEM, and BET. Hydrogen a/d kinetics of $LiBH_4$@C-MSU-H nanocomposites was investigated by a volumetric method. The desorption peak temperatures (measured at 2 °C min^{-1} rate) are 339 °C for the undoped $LiBH_4$@C-MSU-H, 328 °C for the $LiBH_4$@C-MSU-H doped with 1 at% Ni and 318 °C for the $LiBH_4$@C-MSU-H doped with 1 at% N nanocomposites. The activation energies of hydrogen desorption for the investigated nanocomposites were obtained from Kissinger plots: 142.7 kJ mol^{-1} for undoped $LiBH_4$@C-MSU-H, 123.8 kJ mol^{-1} for $LiBH_4$@C-MSU-H 1 at% Ni and 119.5 kJ mol^{-1} for $LiBH_4$@C-MSU-H 1 at% N nanocomposites. The catalytic effect on $LiBH_4$ dehydrogenation due to N-doping of nanocarbons is discussed.

Received 16th October 2025,
Accepted 21st February 2026

DOI: 10.1039/d5cp03997e

rsc.li/pccp

1. Introduction

Due to the greenhouse effect caused by the burning of fossil fuels, a top priority for today's society is the development of a non-polluting and sustainable economy. Moreover, fossil fuels could meet society's needs for a limited period of time. Hydrogen, as an energy carrier, represents a non-polluting energy alternative. Storing hydrogen in hydrides is a safe and inexpensive method. Metal hydrides have a hydrogen mass content below 2 wt% H_2. Lithium borohydride, $LiBH_4$, upon decomposition into LiH and B provides an amount of hydrogen equal to 13.8 wt% H_2, well above the 7 wt% H_2 obtained for magnesium hydride or sodium alanate $NaAlH_4$.[1] Unfortunately, for the rehydrogenation of $LiBH_4$ after hydrogen desorption, very harsh conditions are required, namely 350 atm H_2 at 600 °C.[2]

The difficult absorption/desorption of hydrogen is caused by sluggish kinetics and thermodynamic barriers that negatively influence the dehydrogenation temperature. Significant efforts have been made to improve the hydrogenation/dehydrogenation kinetics of $LiBH_4$ through the use of catalysts such as those described in very recent reviews.[3,4] Another strategy for improving kinetics is nanoconfinement, by embedding borohydrides in various matrices that prevent the growth of hydride grains during hydrogen absorption/desorption cycles, adversely affecting hydrogen diffusion in the hydride bed. For this purpose, various matrices have been used: porous hollow carbon nanospheres,[5] double-layered carbon nanobowls,[6] silica and carbon scaffolds,[7] nanoporous carbon,[8,9] CoNi doped hollow carbon networks,[10] carbon wrapped Fe_3O_4 nanospheres,[11] TiO_2 decorated porous carbonaceous networks,[12] N-doped carbon nanosheets embedded with Co nanoparticles,[13] and Ni nanoparticles coated with porous hollow carbon micropheres.[14] Also mixing with carbon nanotubes[15] or 2D structures like graphene

National Institute of Materials Physics, Atomistilor Str. 405A, 077125, Magurele, Romania. E-mail: petru.palade@infim.ro

doped with FeF_2/FeO_x[16] or high entropy oxide nanoplates[17] have proved to be useful in avoiding the growth of borohydride grains and improving hydrogenation/dehydrogenation kinetics. An interesting approach was to synthesize nanoparticles of $LiBH_4$ supported on Ni doped graphene.[18] Thermodynamic barriers can be reduced through thermodynamic destabilization, which means lowering the decomposition enthalpy by creating new compounds that stabilize the dehydrogenated state as an alternative to the decomposition reaction of $LiBH_4$ into LiH and B.[19] For $LiBH_4$ containing composites, thermodynamic destabilization has been achieved through the systems: $LiBH_4/MgH_2$,[19] $LiBH_4/LiAlH_4$,[20] $LiBH_4/YH_3$,[21] $LiBH_4/Mg_2NiH_4$.[22]

The interaction between $LiBH_4$ and the carbon matrix or between multi-component systems based on lithium borohydride was investigated using modern methods such as *in situ* X-ray Raman spectroscopy[23] and QENS (quasielastic neutron scattering and neutron vibrational spectroscopy),[24] whereas the identification of poorly crystallized phases and reaction mechanisms can be explored by ^{11}B magic angle spinning (MAS) nuclear magnetic resonance.[25]

Both Ni catalysis and $LiBH_4$ nanoconfinement have a synergistic effect on the reversible absorption/desorption of hydrogen.[26] Nitrogen-doped nanoporous carbon has proven to be a very effective support for catalytic reactions or for hydrogen storage[27,28] and has had a significant effect on improving the absorption/desorption kinetics of hydrogen for MgH_2 confined in such matrices.[29] Besides the physicochemical catalytic mechanism, carbon facilitates thermal conduction in the hydride mass (usually having low thermal conductivity), which enhances the hydrogen desorption kinetics (endothermic reaction).

Very recently, solar-driven reversible hydrogen storage was proposed as an efficient technique to generate H_2 reversibly, without using any external heat source, except for solar radiation. MgH_2 was catalyzed with Cu nanoparticles distributed on MXene nanosheets, having a dual effect: (i) photothermal effect under solar radiation and (ii) catalytic effect on hydrogenation/dehydrogenation of MgH_2. Such a system can reversibly store 5.9 wt% H_2 using only solar radiation as the heat source.[30] A similar system using MgH_2 catalyzed with flower-like microspheres made from N-doped TiO_2 nanosheets coated with TiN nanoparticles has a hydrogen storage capacity of 6.1 wt% H_2.[31] Mg_2Ni(Cu) and its hydrogenated compound exhibit intra/interband transitions generating 85% light absorption across the entire spectrum range raising the surface temperature of MgH_2 to 261.8 °C under a light intensity of 2.6 W cm^{-2}. $Mg_2Ni(Cu)/Mg_2Ni(Cu)H_4$ acts as a light-enhanced ''hydrogen pump'' for MgH_2 having both photothermal and catalytic effects, leading to a reversible hydrogen storage amount of 6.1 wt% H_2 with 95% retention under 3.5 W cm^{-1}.[32] MgH_2 catalyzed using a TiO_2/Fe_2O_3 heterojunction photocatalyst releases 3.1 wt% H_2 within 45 min under a light intensity of 1.78 W cm^{-2}, exhibiting a dehydrogenation activation energy of 77.3 kJ mol^{-1}.[33] Among other hydrides, $LiBH_4$ catalyzed using g-C_3N_4/Fe_2O_3 heterojunctions can desorb 2.70 wt% H_2 very quickly within 1 min and 3.87 wt% in 30 min under a light intensity of 1.78 W cm^{-2}.[34] A Ni/ZrO_2 catalyst derived from metal–organic frameworks has been proven useful both for solar-driven hydrogen storage and photothermal conversion of CO_2 to CH_4.[35] Reversible solar-driven hydrogen absorption/desorption of 4.9 wt% H_2 was achieved for the sodium cyclohexanolate/phenoxide pair with 99.9% conversion and selectivity. The initial dehydrogenation rate was 23.4 mmol H_2 g^{-1} h^{-1} (*i.e.* 2 orders of magnitude higher than that obtained *via* thermocatalysis).[36]

The present work investigates the catalytic efficiency of nitrogen and respectively nickel as doping elements for ordered nanoporous carbon on the hydrogenation/dehydrogenation reaction of $LiBH_4$@doped nanoporous carbon nanocomposites. *Via* thermal treatment of the ordered nanoporous carbon matrix in gaseous ammonia, nitrogen doping of carbon exhibiting a strong catalytic effect in improving the kinetics of the hydrogen absorption/desorption reactions is achieved. The amount of nitrogen and its chemical proximity in the structure of the nanoporous carbon were carefully investigated through X-ray photoelectron spectroscopy. The Ni-doped ordered nanoporous carbon was obtained by reduction of Ni-salts deposited within the nanocarbon structure. The modification of the nanoporous carbon structure *via* thermal treatment in ammonia was analyzed through morphological and porosity investigations. The present work presents a comparison between the catalytic efficiency of C–MSU-H doped with the same amount of either N or Ni for improving the hydrogenation/dehydrogenation kinetics of $LiBH_4$ demonstrating the superiority of N over Ni. This will be very useful for replacing the critical or toxic metal in the hydrogenation/dehydrogenation catalyst. We have comparatively discussed the origin of the catalytic effect for Ni and N doping. To our knowledge, this is the first time such a comparison (keeping the same amount of N and Ni dopants) has been carried out.

2. Experimental

2.1 Synthesis of materials

In order to obtain functionalized nanoporous carbon–hydride nanocomposites, the nanoporous carbon was prepared as a replica of nanoporous silica with an ordered structure. Then it was functionalized by treating in gaseous ammonia or by depositing metal ions, followed by chemical reduction. Nanoporous silica with ordered hexagonal pores was obtained starting from cheap precursors (sodium silicate). To obtain MSU-H,[37–39] sodium silicate solution (27% SiO_2, 14% NaOH) (Sigma Aldrich, extra pure) and pluronic surfactant P123 (Sigma Aldrich, average $M_n \sim 5800$ block copolymers PEG–PPG–PEG) were used in the stoichiometric molar ratio 1 SiO_2 : 0.017 P123 : 0.83 CH_3COOH : 0.78 NaOH : 230 H_2O. Thus, 1.2 g of P123 were mixed with 10 mL of 1.0 M acetic acid solution and 10 mL of water. To this microemulsion were added 2.7 g of sodium silicate solution (27 wt% SiO_2 and 14 wt% NaOH) and 30 mL H_2O. The resulting product was stirred for 24 hours at ambient temperature. Subsequently, it was treated at 100 °C for 24 h. The product was filtered and dried and finally the

remaining surfactant was removed by calcination in air at 550 °C for 5 h. The carbon replica of MSU-H, named in the following C-MSU-H,[40] was made by impregnating sucrose solution into the MSU-H matrix in two reaction steps. In the first step, 4 g of nanoporous silica MSU-H were dispersed in a solution consisting of 20 g H_2O and 0.64 g H_2SO_4 (the acid is the catalyst). Then, 5 g of sucrose (carbon source) were added to the formed mixture so that the solution filled the pores of MSU-H. The slurry was heated in an oven for 6 h at 100 °C followed by another 6 h at 160 °C so that the sucrose became polymerized. After that, in the second impregnation step 3.2 g of sucrose and 0.36 g of H_2SO_4 dissolved in 20 g of water were added. The heating in the oven was repeated for 6 h at 100 °C followed by another 6 h at 160 °C so that the sucrose became polymerized and completely filled the MSU-H pores. The product obtained was washed of impurities, filtered and subsequently calcined for 3 h at 400 °C and 4 h at 900 °C in a nitrogen flow (N_2, purity 99.999%) to transform sucrose into carbon. Thereby, a carbon–SiO_2 composite was obtained. The removal of SiO_2 was done *via* treatment with an aqueous solution of 10% hydrofluoric acid and washing with double distilled water until neutral pH. A treatment in gaseous ammonia flow (NH_3, purity 99.999%) with a rate of 100 ml min^{-1} for 4 h was performed on the nanoporous carbon C-MSU-H in order to achieve the doping with N atoms. Special precautions were taken the ammonia being neutralized at the outlet of the heating system. The treatment temperatures were 400 °C, 450 °C and 500 °C.

Besides nitrogen doping, another functionalization procedure of C-MSU-H involved doping with nickel ions. A level of 1 at% Ni doping of nanoporous carbon was envisaged, which meant 4.65 wt% Ni in carbon in order to keep the same doping level previously obtained for N doped C-MSU-H. For this purpose, 0.233 g of nickel nitrate hexahydrate $Ni(NO_3)_2{\cdot}6H_2O$ (Sigma Aldrich > 99.9% trace metal basis) (corresponding to 0.047 g of Ni) dissolved in 10 ml of absolute ethanol was used to impregnate 1 g nanoporous carbon by the incipient wetness method (6 steps). Using this method we obtained a loading of 4.65 wt% Ni/nanoporous carbon (respectively 1 at% Ni/nanoporous carbon). After drying at 70 °C for 10 hours, the nanoporous carbon impregnated with an ethanol solution of $Ni(NO_3)_2{\cdot}6H_2O$ was treated in a 5% H_2/Ar (purity 99.999%) flow (100 ml min^{-1}) for 4 h at 430 °C. Subsequently, nanoporous carbon doped either with N or Ni was mixed with $LiBH_4$ in a proportion of 50/50 wt% and the nanocomposites were synthesized by the melt infiltration under hydrogen pressure of 100 atm at 300 °C, so that $LiBH_4$ (melting temperature 278 °C) infiltrates into the ordered pores of doped C-MSU-H. This method produces $LiBH_4$@(Ni or N) doped C-MSU-H nanocomposites, avoiding the growth of $LiBH_4$ grains during hydrogen absorption/desorption cycles, which would worsen the hydrogenation/dehydrogenation kinetics. Additionally, the heat transfer in the hydride mass was improved. The processing of hydrides was done in a Labstar Mbraun glove box (Garching, Germany) in a controlled atmosphere (<1 ppm of oxygen and moisture) in order to avoid sample contamination.

2.2 Characterization methods

X-ray diffraction measurements were performed using an Anton Parr diffractometer with Cu K-alpha radiation starting from very small angles for pristine ordered nanoporous carbon and respectively nitrogen doped samples with a step of 0.02° in the 2θ range of 0.1–60°. XRD measurements were performed in the 2θ range of 15–80° for $LiBH_4$@ordered nanoporous carbon nanocomposites.

FTIR measurements were performed on pressed pellets containing 120 mg KBr and the IR-active material. To avoid contamination, the powders were ground in a MBraun Labstar glove box. Measurements were performed in the wavenumber range of 300–4000 cm^{-1} using a JASCO-6600 FTIR spectrometer with a measuring step of 4 cm^{-1}.

Nitrogen physisorption analysis was performed at −196 °C using a Micromeritics 3FLEX apparatus. Before determining the surface area, all powders were degassed at 200 °C for 4 h. The Brunauer–Emmett–Teller (BET) formalism was used to calculate the specific surface area from the data acquired at P/P_0 between 0.025 and 0.3. The pore size distribution of the samples was determined from the desorption branch of the N_2 isotherm. The pore size and volume analysis were calculated using the Barrett–Joyner–Halenda (BJH) formalism.

XPS (X-ray photoelectron spectroscopy) measurements were performed using a SPECS spectrometer based on a PHOIBOS 150 analyzer with a monochromatic X-ray source of 300 W with Al Kα radiation—1486.61 eV. Charge compensation was done using a Specs FG15/40 flood gun. The XPS core level lines were recorded using a pass energy of 20 eV while the survey spectra were recorded with a pass energy of 50 eV. The fittings were performed using Spectral Data Processor software using Voigt functions and usual relative sensitivity factors.

TEM images were obtained using a JEM-2100 analytical transmission electron microscope (Jeol, Tokyo, Japan) working at 200 kV endowed with a dispersive X-ray spectrometer. Prior to TEM investigation the samples were dispersed in hexane using an ultrasonic device with high power (VCX 750 Sonics, Newton, CT, USA), followed by drying onto Lacey carbon-coated Cu TEM grids.

Hydrogen storage kinetics measurements were performed using a commercially available Sievert (volumetric) apparatus built by Advanced Material Corporation, Pittsburgh, USA.

3. Results and discussion

3.1 X-ray diffraction

For the pristine ordered nanoporous carbon C-MSU-H and nanoporous carbon samples thermally treated in ammonia flow at 400 °C and 500 °C a hexagonal structure is observed with peaks at very low angles in the X-ray diffraction pattern provided in Fig. 1. The reflections at (1 0 0), (1 1 0) and (2 0 0) indicate a hexagonal lattice constant a = 10.9 nm. The peaks (0 0 2) and (1 0 0) from 2θ of about 23° and 43°, respectively, correspond to a graphitic phase in a very small amount with a lattice constant close to that of pure graphite. This phase

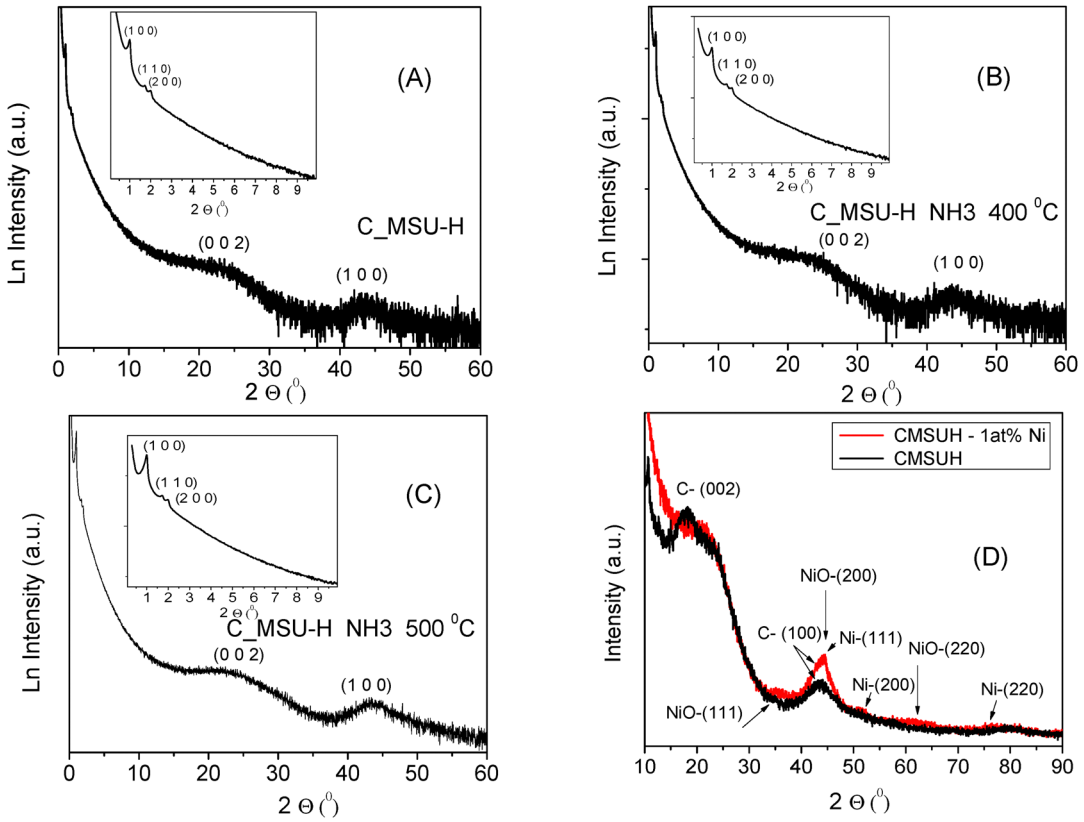

Fig. 1 X-ray diffraction spectra of ordered nanoporous carbon C-MSU-H: (A) as obtained, (B) treated in ammonia gas at 400 °C, (C) treated in ammonia gas at 500 °C and (D) C-MSU-H doped with 1 at% Ni.

appears in a significantly higher amount for the sample treated at 500 °C. The initially ordered nanoporous carbon C-MSU-H was functionalized either by treatment in a flow of gaseous ammonia or by doping with Ni ions. The XRD pattern of C-MSU-H doped with 1 at% Ni (Fig. 1D) exhibits differences from the undoped one due to the presence of very broad peaks corresponding to Ni and NiO which show very small crystallite size of a few nanometers.

The X-ray diffraction spectra for the re-hydrogenated (after cycles of hydrogen absorption/desorption) nanocomposites – 50 wt% $LiBH_4$ – 50 wt% C-MSU-H (named $LiBH_4$@C-MSU-H) (Fig. 2A) and 50 wt% $LiBH_4$ – 50 wt% C-MSU-H doped with 1 at% N (named $LiBH_4$@C-MSU-H 1 at% N) (nitrogen doping level was measured from XPS) (Fig. 2B) are very similar, and show mainly $LiBH_4$ (ICDD file 01-084-8599) and a small amount of LiH (ICDD file 04-013-9487) according to the hydrogen generation reaction:

$$LiBH_4 \leftrightarrow LiH + B + 3/2H_2 \quad (1)$$

Boron cannot be detected in the XRD pattern due to amorphous state.

A relatively small amount of Li_3BO_3 (ICDD file 00-018-0718) can be seen in the XRD pattern, probably appeared during the diffraction measurements, although we mounted a protective foil over the sample. The most important amorphous contribution is due to $LiBH_4$ at $2\theta \approx 25^\circ$, but some amount of $LiBH_4$ crystallizes outside of the ordered nanoporous carbon matrix during the hydrogen absorption/desorption cycles. The X-ray diffraction spectrum for the rehydrogenated composites 50 wt% $LiBH_4$ – 50 wt% C-MSU-H doped with 1 at% Ni (named $LiBH_4$@C-MSU-H 1 at% Ni) (Fig. 2C) presents novel elements compared to the previous ones. Thus, the presence of nickel borides with different percentages of B is observed, namely Ni_3B (ICDD file 00-048-1223) and Ni_2B (ICDD file 00-048-1222) in addition to the $LiBH_4$, LiH and Li_3BO_3 phases. There is no evidence of metallic Ni or NiO in the XRD pattern, probably due to the reduction effect of $LiBH_4$ and the affinity of Ni to the reaction with boron provided from $LiBH_4$.

3.2 FTIR spectroscopy

The measurements were performed in the wavenumber range of 300–4000 cm^{-1} using a JASCO-6600 FTIR spectrometer with a measuring step of 4 cm^{-1} for both the initial C-MSU-H and $LiBH_4$ and for the $LiBH_4$@C-MSU-H and $LiBH_4$@C-MSU-H 1 at% N rehydrogenated nanocomposites as shown in Fig. 3.

The band at 1568 cm^{-1} corresponds to the stretching mode of the carbon atoms in the aromatic ring (C=C) that exists in C-MSU-H. The band at 1036 cm^{-1} in C-MSU-H corresponds to the stretching mode for the C–O interaction, and the band at 3445 cm^{-1} can be assigned to the stretching mode for the O–H bond that appears due to hygroscopicity of KBr.

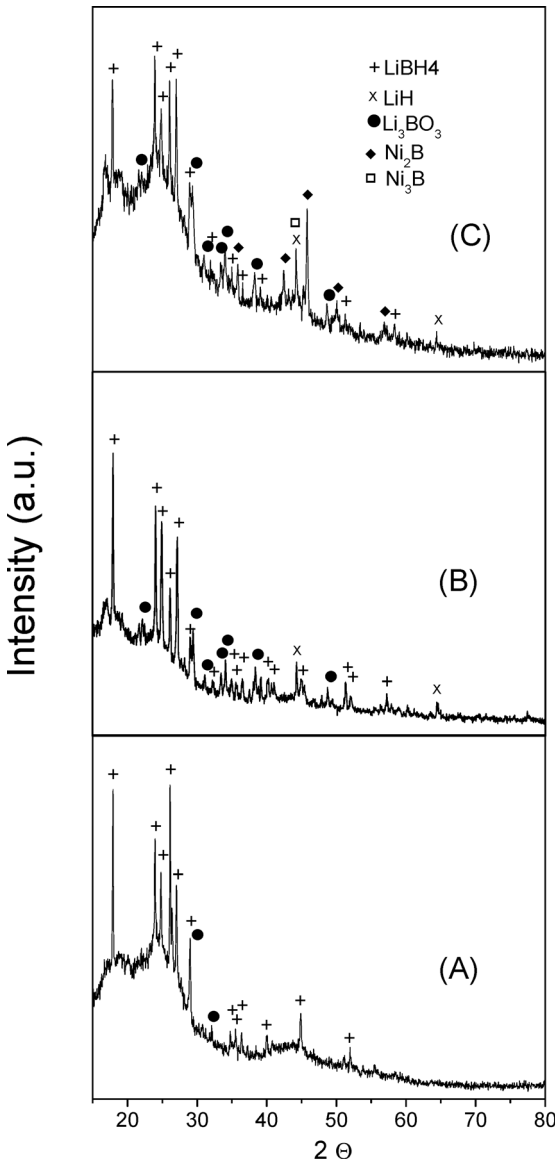

Fig. 2 X-ray diffraction spectra of rehydrogenated nanocomposites: (A) 50 wt%$LiBH_4$ – 50 wt% C-MSU-H ($LiBH_4$@C-MSU-H), (B) 50 wt%$LiBH_4$ – 50 wt% 1 at% N-doped C-MSU-H ($LiBH_4$@C-MSU-H 1 at% N), (C) 50 wt% $LiBH_4$ – 50 wt% 1 at% Ni-doped C-MSU-H ($LiBH_4$@C-MSU-H 1 at% Ni).

The vibrational bands at 2390, 2294 and 2226 cm^{-1} present in $LiBH_4$@C-MSU-H correspond to the stretching mode for the B–H bond in $LiBH_4$. The band at 1126 cm^{-1} can be assigned to the bending B–H vibration in the original $LiBH_4$ and $LiBH_4$@C-MSU-H re-hydrogenated nanocomposites. In $LiBH_4$@C-MSU-H nanocomposites, bands corresponding to the O–H (3440 cm^{-1}), C═C (1572 cm^{-1}) and C–O (1004 cm^{-1}) stretching vibrations also appear, originating from the initial C-MSU-H. Similar to X ray-diffraction, the FTIR spectra proved that after re-hydrogenation the $LiBH_4$ phase is recovered. In the FTIR spectra of the rehydrogenated nanocomposites (Fig. 3) there is no evidence of $Li_2B_{12}H_{12}$ whose distinctive feature would be the band at 2485 cm^{-1}. Borane is not released below 450 °C for $LiBH_4$ infiltrated in nanoporous carbon.[41] We consider that the incomplete hydrogenation is caused by a kinetic barrier. The FTIR spectrum of $LiBH_4$@C-MSU-H is very similar to that of $LiBH_4$@C-MSU-H 1 at% N reydrogenated nanocomposites. There is no obvious change in the FTIR spectra due to the presence of N. This can be understood as being due to the very low nitrogen content in the sample. As expected, the XRD pattern of $LiBH_4$@C-MSU-H 1 at% N is very similar to that of undoped $LiBH_4$@C-MSU-H (Fig. 2). The reason why the presence of nickel borides can be detected in the XRD pattern of $LiBH_4$@C-MSU-H 1 at% Ni rehydrogenated nanocomposites is the much higher atomic scattering factor of Ni compared to that of N, C, B and Li. However, we performed N 1s HRXPS (with a noisy spectrum due to very low N content) on $LiBH_4$@ C-MSU-H 1 at% N rehydrogenated sample showing the presence of Li_3N/Li_3BN_2.

3.3 X-ray photoelectron spectroscopy

We performed X-ray photoelectron spectroscopy on C-MSU-H undoped and doped with nitrogen by thermal treatment under ammonia flow in order to find the amount and chemical state of N embedded in the carbon nanostructure (Table 1). We also performed XPS on Ni doped samples.

The reference energy was taken as the C 1s line C═C bonds, which we set at 284 eV. The spectra from each sample were calibrated according to this reference. The samples have very few contaminants. Other elements, apart from C, O and N, were not observed in the samples. Monotonic increase in the amount of nitrogen is observed with increasing treatment temperature in NH_3 (about 1 at% N doping for 4 h NH_3 at 500 °C). A decrease in the O content is observed following treatment in NH_3. In Fig. 4A–D are depicted the extended XPS spectrum and HRXPS C 1s, O 1s and N 1s spectra for nanoporous carbon sample without N doping. In C 1s HRXPS spectrum (Fig. 4B and Table 2) the binding energy of 284.00 eV corresponds to C-sp^2 from the hexagonal carbon ring from nanoporous ordered structure, binding energy of 285.07 eV can be assigned to C–C, C–H, single bonds, binding energy of 286.43 eV indicates very likely C–O–C bonds, binding energy of 288.29 eV indicates C═O double bonds, whereas binding energy of 290.20 eV can be assigned to specific shake-up C sp^2-π–π^* transition.[42–44] In HRXPS O 1s spectrum (Fig. 4C and Table 3) the binding energy of 531.17 eV indicates molecular O_2 adsorbed or C═O double bonds, whereas the binding energy of 532.86 eV can be assigned to C–O single bonds.[44] In HRXPS N 1s spectrum for C-MSU-H – NH_3 (4 h, 500 °C) (sample doped with $\approx$ 1 at% N) (Fig. 4E and Table 4) the binding energy of 397.94 eV indicates N in the pyridinic position whereas the binding energy of 399.35 can be assigned to N in the pyrrolic position.[42,45]

An increase in the C-sp^2 content is observed with increasing treatment temperature in ammonia flow for C-MSU-H (Table 2). A decrease in the content of adsorbed oxygen and/or C═O bonds and an increase in the content of C–O bonds is observed following the thermal treatment in NH_3 (Table 3). An increase in the N-pyridinic content and a decrease in the N-pyrrolic content are observed as a result of increasing the treatment

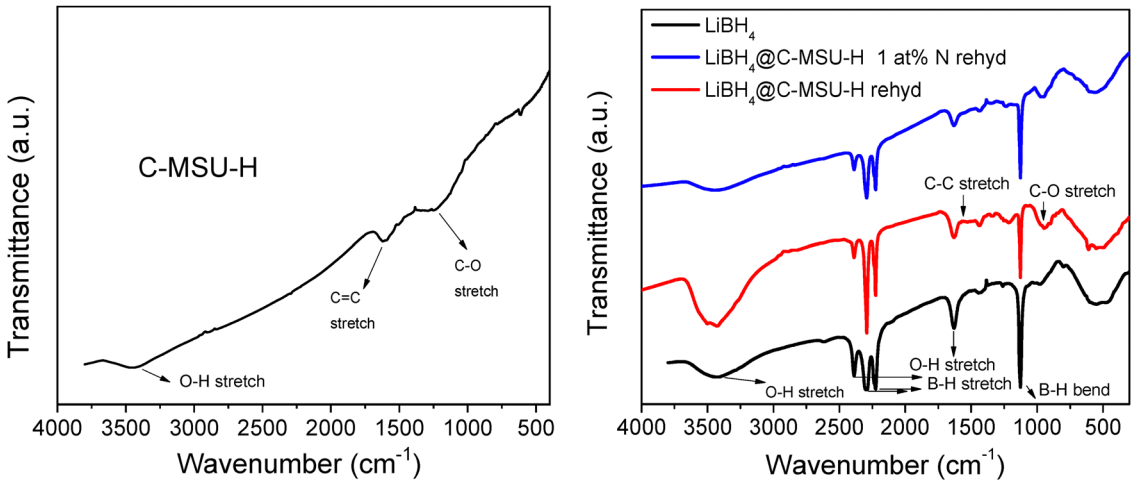

Fig. 3 FTIR spectra of C-MSU-H and the original $LiBH_4$ and $LiBH_4$@C-MSU-H and $LiBH_4$@C-MSU-H 1 at% N rehydrogenated nanocomposites.

Table 1 The composition of nanoporous carbon as derived from X-ray photoelectron spectroscopy

Sample	C (at%)	O (at%)	N (at%)
C-MSU-H pristine	96.5	3.5	—
C-MSU-H treated 4 h NH_3 at 400 °C	96.8	2.6	0.6
C-MSU-H treated 4 h NH_3 at 450 °C	96.9	2.4	0.7
C-MSU-H treated 4 h NH_3 at 500 °C	96.5	2.6	0.9

temperature in gaseous ammonia (Table 4). However, C-MSU-H thermally treated in NH_3 samples have a majority of nitrogen atoms into pyrrolic configurations. The nitrogen atoms incorporated into graphitic, pyridinic, or pyrrolic configurations modify the local electronic density and create electron-rich regions that can interact strongly with the metal cations of the hydride (*e.g.*, Li^+, Na^+, Mg^{2+}). These interactions lead to polarization of the Li–H bonds within the hydride, weakening them and lowering the activation energy for hydrogen desorption.[46] Consequently, N-doped carbons not only provide physical confinement but also exert a catalytic effect on hydrogen release. The degree of doping and the type of nitrogen species play a decisive role in tuning these effects: graphitic N enhances conductivity and stabilizes the framework, while pyridinic and pyrrolic N sites provide strong chemical anchoring and catalytic reactivity. The theoretical simulations further demonstrate that N-doped sp^2/sp^3 hybrid carbon can migrate the Fermi level to the conduction band, leading to an n-type conductivity due to the additional electrons attributed to the N dopant.[47] Particularly, pyridinic nitrogen from C-MSU-H thermally treated in ammonia has a strong catalytic effect. In this state, the N atom is sp^2 hybridized with carbon atoms from the 2D hexagonal aromatic ring, participating in one π and two σ bonds with the nearest neighboring carbon atoms, providing a lone pair of electrons available for additional bonding. Pyridinic nitrogen embedded in the nanoporous carbon scaffold could act as a Lewis base and donate significant electron density to the confined hydride layered onto the scaffold's surface with an effect on hydride thermodynamic destabilization. XPS data confirm the pyridinic and pyrrolic nitrogen in our prepared N-doped C-MSU-H nanocarbons and the catalytic activity of such supports is expected to be higher than that of neat C-MSU-H as we will further notice from hydrogen storage behavior. The HRXPS N 1s spectrum of 50 wt% $LiBH_4$–50 wt% 1 at% N-doped C-MSU-H rehydrogenated nanocomposites (noted as $LiBH_4$@C-MSU-H 1 at% N) is depicted in Fig. 4F. The majority peak corresponding to binding energy of 397.2 eV can be attributed to the formation of Li_3N or Li_3BN_2, both having binding energies close to 397 eV.[48–50] The binding energy given in the literature for Li_2NH is 398.2 eV,[51] which is significantly higher than that of our experimental value. In the Ni $2p_{3/2}$ HRXPS spectrum for 1 at% Ni-doped C-MSU-H (Fig. 4G) the binding energy of 852.63 eV corresponds to Ni metal, the binding energy of 854.31 eV can be assigned to the Ni^{2+} oxidation state which belongs to NiO, and the binding energy of 855.91 eV corresponds to a higher oxidation state of Ni^{4+} which can be assigned to NiO_2. In Ni $2p_{3/2}$ HRXPS for $LiBH_4$@C-MSU-H 1 at% Ni re-hydrogenated nanocomposites (Fig. 4H) the binding energy of 852.96 eV can be assigned to Ni–B bonds.[52,53]

3.4 TEM investigation

The transmission electron microscopy image for as prepared C-MSU-H sample is presented in Fig. 5A. The size of the hexagonal nanopores of the ordered structure is approximately 4 nm. It can also be observed that in the case of the C-MSU-H thermally treated in NH_3 flow at 500 °C (Fig. 5B), the ordered structure remains similar to the untreated C-MSU-H sample, with hexagonal nanopores of almost the same size. In Fig. 5C are shown TEM images at various magnifications for C-MSU-H decorated with Ni nanoparticles. The samples indicate an ordered nanoporous carbon structure with uniformly distributed Ni/NiO clusters, without agglomeration. In the EDAX spectrum (Fig. 5D) taken over a large area where nanoparticles are present, a maximum corresponding to nickel is observed and the composition of the nanoparticles is confirmed. The nanoparticles are uniformly distributed in the structure, as can be seen from Fig. 5C. The histogram corresponding to their size

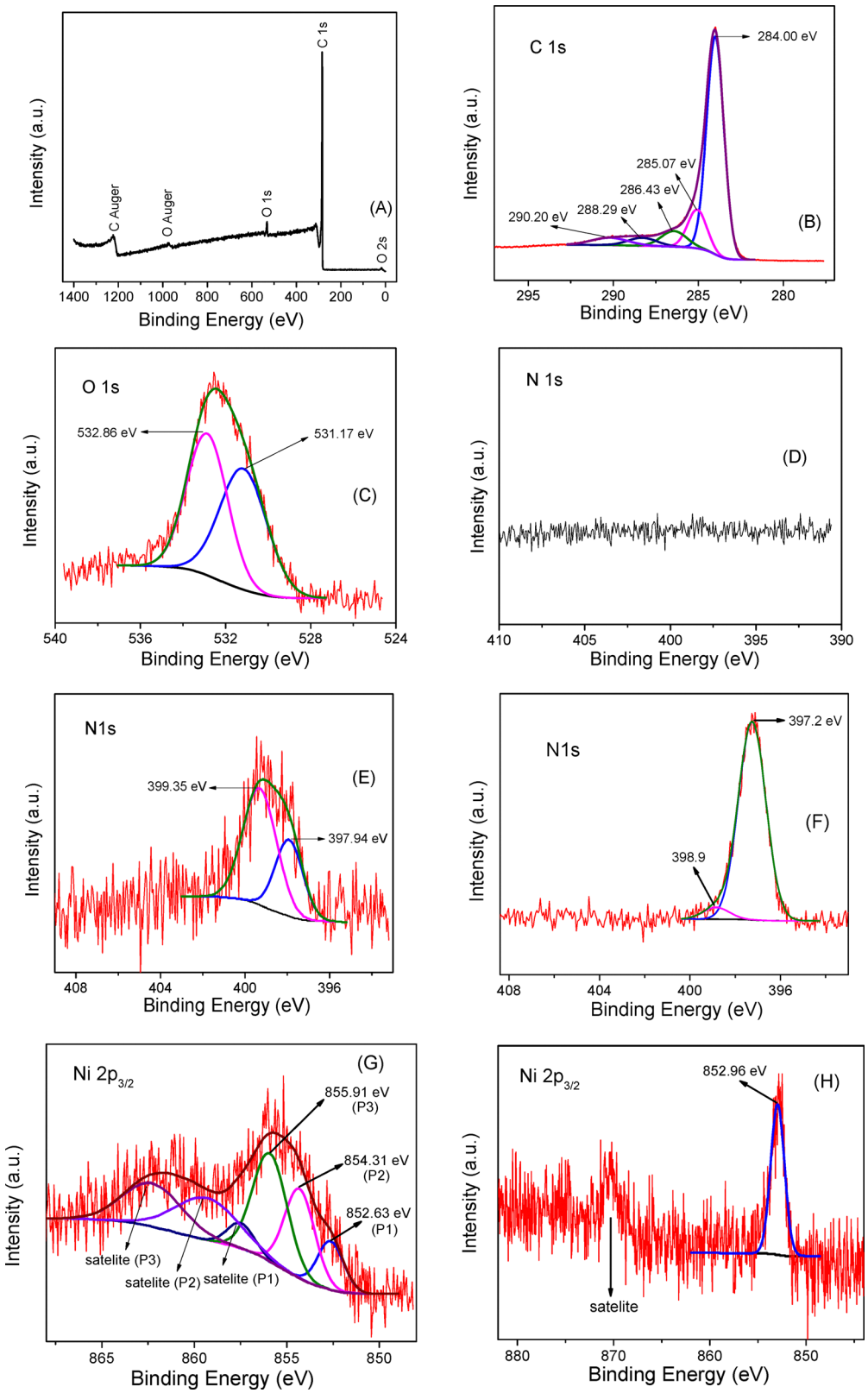

Fig. 4 X-ray photoelectron spectra (XPS) for whole binding energy range (A) and high resolution X-ray photoelectron spectra (HRXPS) for C 1s (B), O 1s (C) and N 1s (D) for pristine C-MSU-H ordered nanoporous carbon sample and N 1s HRXPS for 1 at% N-doped C-MSU-H (E) and N 1s HRXPS for $LiBH_4$@C-MSU-H 1 at% N rehydrogenated nanocomposites (F) and Ni $2p_{3/2}$ HRXPS for 1 at% Ni-doped C-MSU-H (G) and Ni $2p_{3/2}$ HRXPS for $LiBH_4$@C-MSU-H 1 at% Ni rehydrogenated nanocomposites (H).

Table 2 HRXPS C 1s fitting results (binding energies and concentrations corresponding to subspectra) for nanoporous carbon samples treated at various temperatures in ammonia flow

	C-sp^2		C–C, C–H, C–N		C–O–C		C═O		C sp^2-π–π* shake up	
Sample	BE (eV)	Conc. (at%)	BE (eV)	Conc. (at%)	BE (eV)	Conc. (at%)	BE (eV)	Conc. (at%)	BE (eV)	Conc. (at%)
C-MSU-H	284.0	69.70	285.07	13.70	286.43	7.40	288.29	4.20	290.2	5.00
C-MSU-H 4 h/400 °C	283.9	69.60	285.15	13.00	286.48	7.40	288.42	5.00	290.4	5.10
C-MSU-H 4 h/450 °C	284.0	73.80	285.00	13.90	286.16	5.00	287.48	3.00	289.6	4.30
C-MSU-H 4 h/500 °C	284.0	76.30	285.18	12.80	286.60	5.50	288.48	2.90	290.1	2.40

Table 3 HRXPS O 1s fitting results (binding energies and concentrations corresponding to subspectra) for nanoporous carbon samples treated at various temperatures in ammonia flow

	O ads, C═O		C–O	
Sample	BE (eV)	Conc. (at%)	BE (eV)	Conc. (at%)
C-MSU-H	531.17	49.60	532.86	50.40
C-MSU-H 4 h/400 °C	530.88	41.00	532.82	59.00
C-MSU-H 4 h/450 °C	531.11	25.40	532.61	74.60
C-MSU-H 4 h/500 °C	531.06	36.40	532.65	63.60

Table 4 HRXPS N 1s fitting results (binding energies and concentrations corresponding to subspectra) for nanoporous carbon samples treated at various temperatures in ammonia flow

	N-pyridinic		N-pyrrolic	
Sample	BE (eV)	Conc. (at%)	BE (eV)	Conc. (at%)
C-MSU-H	—	—	—	—
C-MSU-H 4 h/400 °C	398.00	17.10	399.15	82.90
C-MSU-H 4 h/450 °C	397.92	34.90	399.30	65.10
C-MSU-H 4 h/500 °C	397.94	39.60	399.35	60.40

distribution and the lognormal fit is presented in Fig. 5E, indicating a mean diameter of 5.3 nm.

The rehydrogenated sample $LiBH_4$@C-MSU-H 1 at% Ni consists of large amorphous particles containing well-dispersed nanoparticles (Fig. 5F). EDX chemical mapping of the amorphous particles reveals a uniform distribution of B and C, while the nanoparticles are rich in Ni. The nickel distribution appears to be concentrated in the nanoparticles, and the speckles appearing on maps outside of them can be attributed to noise. The rehydrogenated $LiBH_4$@C-MSU-H 1 at% N sample consists of large amorphous particles with irregular shapes that do not show any special features (Fig. 5G). EDX chemical mapping reveals a uniform distribution of B, N, and C throughout the surface of the investigated particles, although the concentration of N is low, close to the detection quantification limit.

3.5 Porosity measurements

The porosity parameters of the samples are summarized in Table 5. The surface area calculated using the BET formalism for the samples C-MSU-H and C–MSU-NH_3 (4 h, 500 °C) is 1264 $m^2\ g^{-1}$ and, respectively, 1198 $m^2\ g^{-1}$ indicating that the ordered nanoporous structure is maintained after the treatment at 500 °C in ammonia gas.

The isothermal N_2 adsorption–desorption plots, shown in Fig. 6(A and C), have isotherms of type IV shape. The pore volume and average pore diameter for the pristine C-MSU-H and C–MSU-NH_3 (4 h, 500 °C) are presented in Fig. 6(B and D) and Table 5 and the values obtained indicate once again the preservation of the nanostructure of the sample after the treatment at 500 °C in NH_3. The combination of nanoporosity and N-doping offers synergistic benefits. The nanoporous network ensures that hydrides are spatially confined, maximizing surface contact with the doped carbon walls, while the doped sites locally destabilize the hydride, effectively lowering both the desorption enthalpy and activation energy. This results in improved hydrogen release at significantly lower temperatures compared to bulk hydrides. Additionally, the carbon host enhances thermal conductivity with positive effect on hydrogen desorption which requires external heating because it is an endothermic reaction and mitigates phase segregation or irreversible decomposition during cycling.

3.6 Hydrogen storage behavior

Hydrogen absorption–desorption measurements were taken using an automated volumetric apparatus (Sievert). We performed isothermal kinetic hydrogen absorption and desorption and thermal programmed desorption measurements. In Fig. 7A, it can be observed that a large amount of hydrogen is released after the first desorption. The theoretical amount of hydrogen reversibly stored in the reaction $LiBH_4 \leftrightarrow LiH + B + 3/2H_2$ is 13.8 wt% H_2. The weight ratio between $LiBH_4$ and C-MSU-H was 1 : 1. That means that the theoretical amount of hydrogen reversibly stored by $LiBH_4$@C-MSU-H should be 6.9 wt% H_2. However, the theoretical reversible amount should be approximately 6.5–6.7 wt% H_2 (less than 6.9 wt% H_2) because nickel borides or Li_3N/Li_3BN_2 are also formed in the rehydrogenated nanocomposites containing either Ni or N. By making nanocomposites of $LiBH_4$ infiltrate under H_2 pressure in ordered nanoporous carbon, the aim is to avoid the growth of $LiBH_4$ grains following the hydrogen absorption–desorption cycles, which would lead to a drastic deterioration of the hydrogen absorption–desorption kinetics. $LiBH_4$@C-MSU-H desorbs 6.2 wt% H_2 up to 450 °C for the first desorption with a temperature ramp of

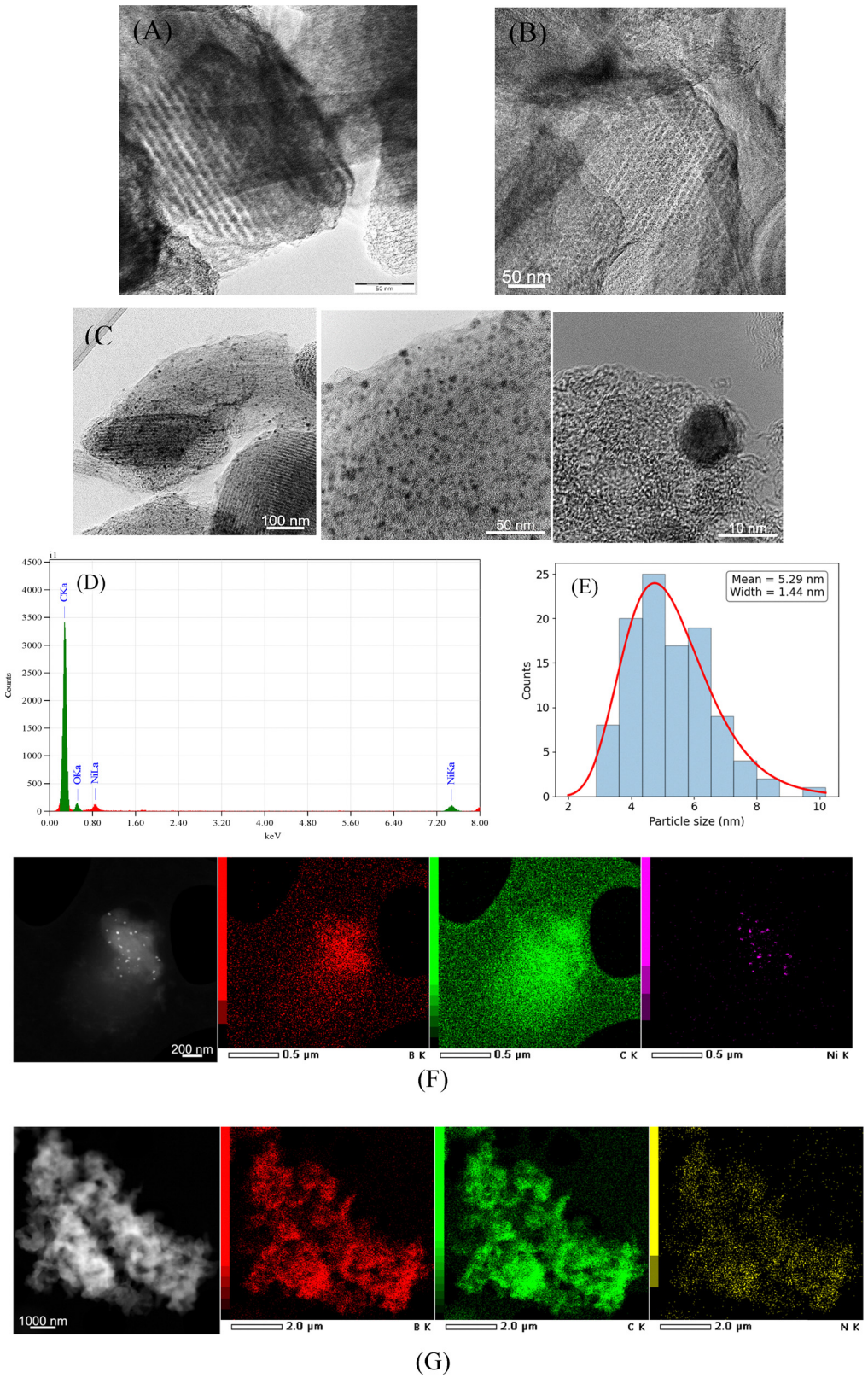

Fig. 5 TEM images for (A) as prepared C-MSU-H, (B) C-MSU-H thermally treated in NH_3 at 500 °C, (C) C-MSU-H decorated with Ni nanoparticles and corresponding EDAX spectrum (D) and histogram of the measured values of the diameter of the Ni nanoparticle with a fitted lognormal distribution, showing the mean and width of the underlying size distribution (E). (F) TEM/EDS mapping of $LiBH_4$@C-MSU-H 1 at% Ni, (G) TEM/EDS mapping of $LiBH_4$@C-MSU-H 1 at% N.

Table 5 Surface area, pore volume, and average pore diameter for as prepared C-MSU-H and C-MSU-H thermally treated in ammonia flow at 500 °C

Sample	Surf. area BET (m^2 g^{-1})	Surf. area BJH ads (m^2 g^{-1})	Surf. area BJH des (m^2 g^{-1})	Pore vol BJH ads (cm^3 g^{-1})	Pore vol BJH des (cm^3 g^{-1})	Pore diam. BJH ads (nm)	Pore diam. BJH des (nm)
C-MSU-H	1264	1126	1197	1.158	1.288	4.113	4.1057
C-MSU-H NH_3, 4 h, 500 °C	1198	1073	1131	1.051	1.105	3.915	3.9078

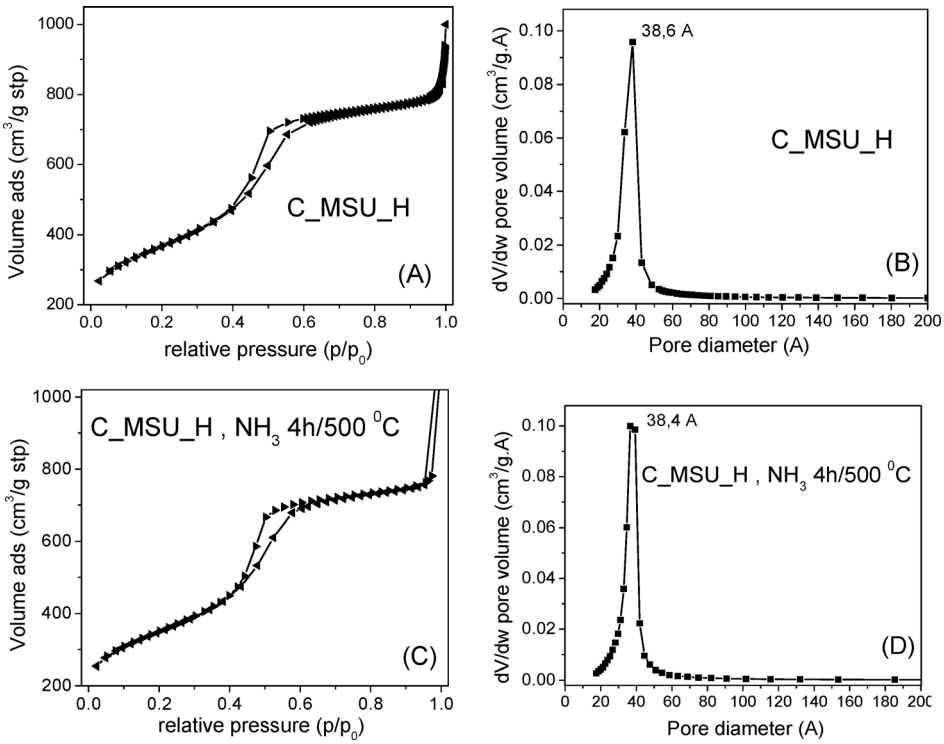

Fig. 6 N_2 adsorption/desorption isotherms and pore size distributions for as-prepared C-MSU-H (A) and (B) and C-MSU-H thermally treated in ammonia flow at 500 °C (C) and (D).

2 °C min^{-1} (Fig. 7A). For complete desorption a much longer desorption time at 450 °C is required. Due to the presence of 1 at% Ni or N as doping elements, the $LiBH_4$@doped C-MSU-H nanocomposites should desorb less than the theoretical amount of 6.9 wt% H_2. $LiBH_4$@C-MSU-H 1 at% Ni desorbs up to 450 °C, the least among all the samples, approximately 5.3 wt% H_2 for the first desorption. After four hydrogen absorption–desorption cycles $LiBH_4$@C-MSU-H releases only 3.1 wt% H_2 up to 450 °C (Fig. 7B). $LiBH_4$–C-MSU-H 1 at% N and $LiBH_4$–C-MSU-H 1 at% Ni samples desorb 4.1 and 3.8 wt% H_2 up to 450 °C, respectively, using the same temperature ramp of 2 °C min^{-1} (Fig. 7B). For complete desorption, a much longer desorption time at 450 °C is required. Faster desorption kinetics is observed for the N-doped sample compared to Ni-doped sample, but both doped samples have much faster desorption kinetics than the sample containing undoped C-MSU-H.

The experimental maximum reversible capacity was determined at 450 °C by allowing hydrogen uptake for at least 20 h under 100 atm and prolonged hydrogen desorption at the same temperature (at least 8 h). Fig. S1 (SI) describes thermal programmed desorption up to 450 °C and prolonged desorption at this final temperature. We obtained a reversible capacity of 6.14 wt% H_2 for $LiBH_4$@C-MSU-H 1 at% N and 6.05 wt% H_2 for $LiBH_4$@C-MSU-H 1 at % Ni rehydrogenated nanocomposites. The amount of hydrogen released after several absorption–desorption cycles is lower than that in the first desorption due to the impossibility of complete rehydrogenation of the dehydrogenated nanocomposites due to a kinetic barrier. Fig. 7C shows the desorption peak temperatures after four absorption/desorption cycles for undoped $LiBH_4$@C-MSU-H nanocomposites and the ones doped with N or Ni. A desorption peak temperature of 339 °C is observed for $LiBH_4$@C-MSU-H, 328 °C for $LiBH_4$@C-MSU-H 1 at% Ni and 318 °C for $LiBH_4$@C-MSU-H 1 at% N, thus a clear advantage for the N-doped nanocomposites compared with the other two samples. Fig. 7D shows the absorption kinetics after 4 a/d cycles for $LiBH_4$ infiltrated in nanoporous carbon containing undoped, N doped and Ni doped C-MSU-H performed at 450 °C and 100 atm H_2. In 40 000 s (approximately 11 h) the $LiBH_4$@C-MSU-H sample absorbs 3.6 wt% H_2, $LiBH_4$@C–MSU-H 1 at%

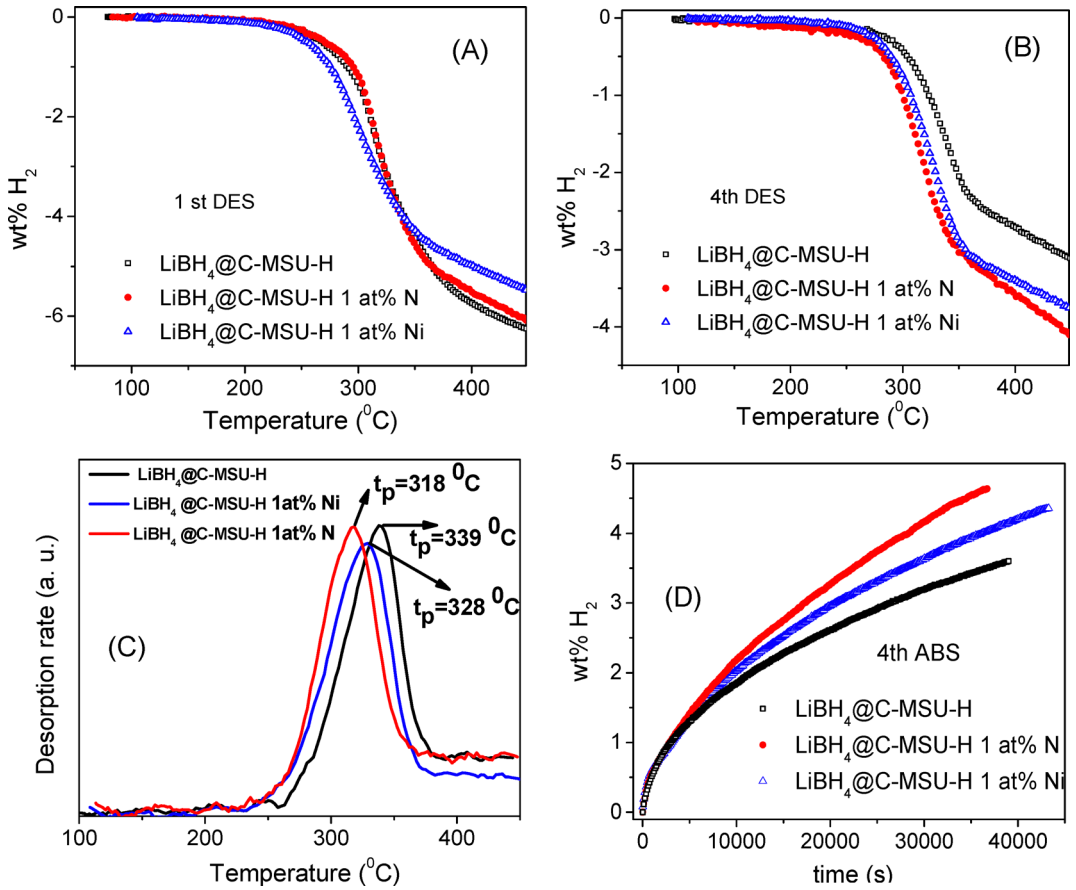

Fig. 7 Thermal programmed desorption with temperature ramp of 2 °C min^{-1} (A – first desorption, B – after 4 cycles of absorption/desorption). (C) Desorption peak temperature (measured for 2 °C min^{-1} heating rate) and (D) absorption kinetics after 4 H_2 absorption/desorption cycles for $LiBH_4$@C-MSU-H, $LiBH_4$@C-MSU-H 1 at% N and $LiBH_4$@C-MSU-H 1 at% Ni. The amount of hydrogen is reported relative to the total weight of the composite (including the weight of the nanoporous carbon).

Ni absorbs 4.3 wt% H_2 and $LiBH_4$@C–MSU-H 1 at% N almost 4.6 wt% H_2. Once again, also regarding the absorption kinetics, N-doped nanocomposites show the best behavior, while undoped nanocomposites behave the worst.

The Kissinger plot[54] allows obtaining the activation energy of hydrogen desorption from the slope of the $\ln(\beta/T_p^2)$ *vs.* $1/T_p$ graph according to the relation

$$E = -R\frac{\mathrm{d}\left(\ln\left(\frac{\beta}{T_p^2}\right)\right)}{\mathrm{d}\left(\frac{1}{T_p}\right)} \quad (2)$$

where β is the heating rate in (°C min^{-1}) and T_p is the desorption peak temperature at different heating rates. The desorption peak temperatures for different heating rates and the related Kissinger linear plots are presented in Fig. 8A–C, from which the activation energies of desorption are extracted. For $LiBH_4$@C-MSU-H we obtained 142.7 kJ mol^{-1}, whereas for $LiBH_4$@C-MSU-H 1 at% Ni we got 123.8 kJ mol^{-1} and the lowest activation energy of 119.5 kJ mol^{-1} was found for $LiBH_4$@C-MSU-H 1 at% N. According to the activation energy of desorption values, $LiBH_4$ infiltrated in C-MSU-H doped with 1 at% N has the fastest hydrogen desorption kinetics among all samples.

The incorporation of Li_3N, $LiNH_2$, or Li_2NH into $LiBH_4$@N-doped mesoporous carbons significantly enhances both hydrogen desorption kinetics and reversibility, primarily *via* the formation of stable Li–B–N–H intermediates and the reduction of activation energy barriers. Within N-doped nanoporous carbons, the dispersion of Li_3N or $LiNH_2$ nanoparticles ensures intimate contact with $LiBH_4$ and maximizes interface area. Nitrogen functionalities on the carbon surface (pyridinic or pyrrolic N) act as Lewis base sites that coordinate to Li^+ ions from $LiBH_4$ or Li_3N, inducing polarization of B–H bonds and facilitating H^- transfer. In confined geometries, this reaction is spatially controlled, producing defect-rich interphases that sustain reversibility by minimizing B segregation and LiH aggregation. During cycling, the $LiNH_2 \leftrightarrow Li_2NH \leftrightarrow Li_3N$ coupled equilibrium acts as a hydrogen reservoir, allowing dynamic hydrogen exchange.[55] Additionally, these equilibria maintain reactive species within the composite, stabilizing the system during multiple hydrogen absorption–desorption cycles.

$$Li_3N + 2H_2 \leftrightarrow Li_2NH + LiH + H_2 \leftrightarrow LiNH_2 + 2LiH \quad (3)$$

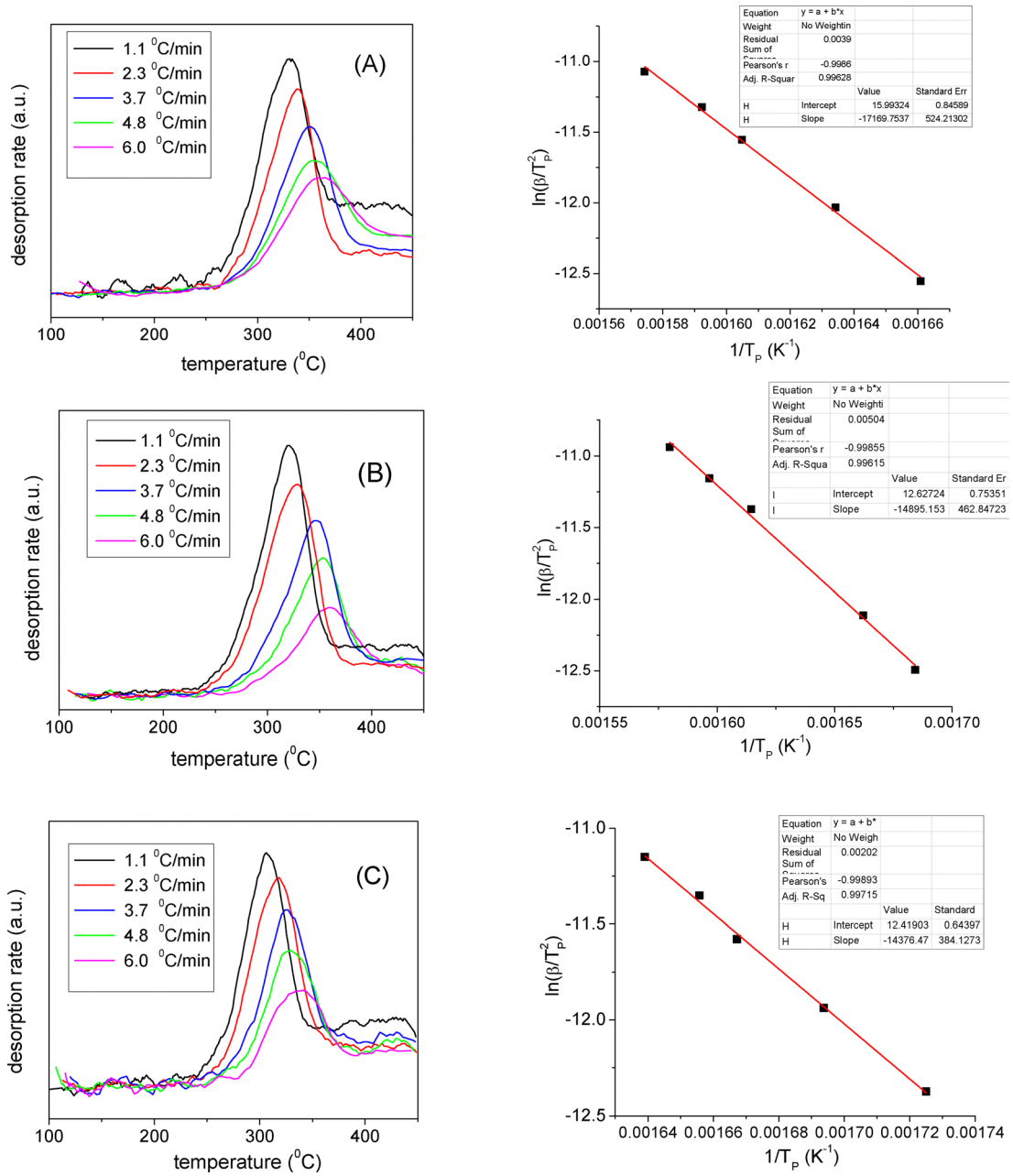

Fig. 8 Desorption peak temperature measured at various heating rates and corresponding Kissinger plots for (A) $LiBH_4$@C-MSU-H, (B) $LiBH_4$@C-MSU-H 1 at% Ni and (C) $LiBH_4$@C-MSU-H 1 at% N.

The underlying chemistry encompasses formation of $Li_4BN_3H_{10}$[56] and its dehydrogenation to another catalytic species, Li_3BN_2.[50] When $LiBH_4$ is mixed or confined with Li_3N, or equivalently with $LiNH_2$ (derived *in situ* from $Li_3N + H_2$), a solid–solid reaction occurs upon heating, yielding the complex hydride $Li_4BN_3H_{10}$:

$$3LiNH_2 + LiBH_4 \rightarrow Li_4BN_3H_{10} \quad (4)$$

This reaction represents a chemical destabilization of $LiBH_4$ through amide/nitride incorporation, resulting in a hydrogen-rich compound (~11.4 wt% H) that can dehydrogenate at lower temperatures (~250 °C). $Li_4BN_3H_{10}$ is the most thermodynamically favorable intermediate in the Li–B–N–H system.[57] Upon heating, it may undergo several reactions leading to Li_3BN_2 as the more probable reaction product according to the reaction[58]

$$Li_4BN_3H_{10} \rightarrow Li_3BN_2 + LiNH_2 + 4H_2 \quad (5)$$

Our HRXPS N 1s spectrum is consistent with the formation of Li_3BN_2 as an active catalytic species in $LiBH_4$

dehydrogenation/rehydrogenation. The catalytic enhancement of $LiBH_4$ hydrogen sorption by Li_3BN_2, can be attributed to the formation and decomposition of the $Li_4BN_3H_{10}$ intermediate, and the interfacial electronic effects induced by N-doped carbon supports. The synergy between $LiBH_4$ and N-doped carbon nanostructures—which provides conductive, confining, and catalytically active environments—yields a composite system with enhanced kinetics, reduced activation energy, and improved reversibility for hydrogen storage applications. Ni as a dopant for C-MSU-H forms catalysts such as Ni_2B and Ni_3B after interaction with $LiBH_4$ which are less efficient than Li_3BN_2. Moreover, Li_3BN_2 catalytic centers formed around nitrogen inside the C-MSU-H matrix are much more dispersed compared to Ni_2B and Ni_3B clusters (provided from Ni/NiO initial clusters of 5.3 nm dispersed onto the C-MSU-H surface), leading to higher catalytic efficiency. Nickel borides actively participate in H_2 dissociation/recombination. Using first principles calculations Liu *et al.*[14] demonstrated that the dissociation energy for removing one H from $LiBH_4$ decreased down to 1.00 eV for $LiBH_4$ on Ni_2B, much lower than the value of 4.22 eV for bulk $LiBH_4$ and even lower than that of $LiBH_4$ on Ni (1.27 eV) showing a superior catalytic effect of nickel boride compared to pure nickel. Additionally, using EXAFS spectroscopy at the Ni K-edge for 5 wt% Ni-catalyzed $LiBH_4$, Ngene *et al.*[59] identified Ni_xB phases with different Ni–B and Ni–Ni coordinations for the dehydrogenated and rehydrogenated samples, which behave reversibly. Specifically, for the dehydrogenated samples Ni–Ni coordination decreased and Ni–B coordination increased whereas for the rehydrogenated samples Ni–Ni coordination increased and Ni–B coordination decreased.

The purpose of the work was to experimentally demonstrate the superiority of N over Ni as a doping element for the C-MSU-H-based catalyst for improving the dehydrogenation kinetics of $LiBH_4$ and to explain this experimental finding. Table S1 (SI) shows the comparison of the hydrogen storage performances of the $LiBH_4$@C-MSU-H 1 at% N studied in the present work with those presented in state-of-the-art literature for $LiBH_4$-based systems. Our material was obtained through a simple procedure (melt infiltration), which does not consume much time and resources such as expensive precursors or toxic and critical elements. Further optimization of the catalyst is required to achieve better performances.

4. Conclusions

Ordered nanoporous carbon with nitrogen substitution was prepared using the nanotemplating method starting from nanoporous silica by sucrose impregnation and pyrolysis followed by etching in HF. Finally, the treatment in a gaseous ammonia flow at temperatures between 400 °C and 500 °C was used for nitrogen doping. For the doping of the ordered nanoporous carbon with 1 at% Ni, nickel nitrate hexahydrate dissolved in absolute ethanol was used. The final thermal treatment was performed for 4 h at 430 °C in a 5% H_2/Ar flow. The ordered carbon nanoporous structure is maintained even after nitrogen doping according to diffraction spectra and TEM images. Doping levels of up to 1 at% are obtained by treatments in a gaseous ammonia flow at 500 °C. For the ordered nanoporous carbon C–MSU-H doped with N, an increase in the N-pyridinic content and a decrease in the N-pyrrolic content are observed as a result of increasing the treatment temperature in gaseous ammonia flow. However, the samples have mostly N-pyrrolic. After nickel doping, homogeneously distributed clusters with average size of 5.3 nm containing Ni and NiO are observed in TEM decorating the ordered nanoporous carbon structure C–MSU-H. Nanocomposites 50 wt% $LiBH_4$–50 wt% undoped or doped with N or Ni ordered nanoporous carbon ($LiBH_4$@C-MSU-H, $LiBH_4$@C-MSU-H 1 at% N, $LiBH_4$@C-MSU-H 1 at% Ni) were prepared using the method of infiltration under hydrogen pressure above the melting temperature of $LiBH_4$. According to XRD, for the re-hydrogenated $LiBH_4$@C-MSU-H 1 at% Ni nickel borides are also observed. The fastest hydrogen absorption and desorption kinetics were obtained for the $LiBH_4$@C-MSU-H 1 at% N, followed by $LiBH_4$@C-MSU-H 1 at% Ni and much slower desorption kinetics for the undoped nanocomposites. The desorption peak temperatures (2 °C min^{-1} ramp) are 339 °C for $LiBH_4$@C-MSU-H, 328 °C for $LiBH_4$@C-MSU-H 1 at% Ni and 318 °C for the $LiBH_4$@C-MSU-H 1 at% N. From the Kissinger plots the activation energies of hydrogen desorption for the nanocomposites were obtained: 142.7 kJ mol^{-1} for $LiBH_4$@C-MSU-H, 123.8 kJ mol^{-1} for $LiBH_4$@C-MSU-H doped with 1 at% Ni and 119.5 kJ mol^{-1} for $LiBH_4$ infiltrated in 1 at% N-doped C-MSU-H.

Author contributions

Conceptualization: P. P. and C. C.; investigation: P. P., C. N., A. G. M., and C. R., formal analysis: P. P., C. C., C. N. A. G. M., and C. R.; software: C. C., P. P., C. R., and C. N.; data curation: P. P. and C. C.; writing original draft: P. P., C. C., C. N., and A. G. M.; writing – revised editing: all authors. All authors have read and agreed to the published version of the manuscript.

Conflicts of interest

There are no conflicts of interest to declare.

Data availability

The data that support the findings of this study are available from the authors upon reasonable request.

Supplementary information (SI) is available. See DOI: https://doi.org/10.1039/d5cp03997e.

Acknowledgements

This work was funded by the Core Program of the National Institute of Materials Physics, granted by the Romanian Ministry of Research, Innovation and Digitization through the Project PC3-PN23080303.

References

1 L. Schlapbach and A. Züttel, Hydrogen-storage materials for mobile applications, *Nature*, 2001, **414**, 353–358.

2 S. Orimo, Y. Nakamori, G. Kitahara, K. Miwa, N. Ohba, S. Towata and A. Züttel, Dehydriding and rehydriding reactions of $LiBH_4$, *J. Alloys Compd.*, 2005, **404–406**, 427–430.

3 Y. Xu, Y. Zhou, Y. Li, M. Ashuri and Z. Ding, Engineering $LiBH_4$-based materials for advanced hydrogen storage: A critical review of catalysis, nanoconfinement, and composite design, *Molecules*, 2024, **29**, 5774.

4 D. Yin, X. Wang, F. Wu, D. Shang, H. Li, P. Huang and L. Zhang, A mini review on the state-of-the-art progress of $LiBH_4$ for hydrogen storage: Challenges and perspectives, *J. Alloys Compd.*, 2025, **1041**, 183883.

5 J. Zheng, Z. Yao, X. Xiao, X. Wang, J. He, M. Chen, H. Cheng, L. Zhang and L. Chen, Enhanced hydrogen storage properties of high-loading nanoconfined $LiBH_4$-$Mg(BH_4)_2$ composites with porous hollow carbon nanospheres, *Int. J. Hydrogen Energy*, 2021, **46**, 852–864.

6 R. Wu, X. Zhang, Y. Liu, L. Zhang, J. Lu, M. Gao and H. Pan, A unique double-layered carbon nanobowl-confined lithium borohydride for highly reversible hydrogen storage, *Small*, 2020, **16**, 2001963.

7 Suwarno, P. Ngene, A. Nale, T. M. Eggenhuisen, M. Oschatz, J. P. Embs, A. Remhof and P. E. de Jongh, Confinement effects for lithium borohydride: comparing silica and carbon scaffolds, *J. Phys. Chem. C*, 2017, **121**, 4197–4205.

8 S. D. House, X. Liu, A. A. Rockett, E. H. Majzoub and I. M. Robertson, Characterization of the dehydrogenation process of $LiBH_4$ confined in nanoporous carbon, *J. Phys. Chem. C*, 2014, **118**, 8843–8851.

9 A. Gasnier and F. C. Gennari, Graphene entanglement in a mesoporous resorcinol-formaldehyde matrix applied to the nanoconfinement of $LiBH_4$ for hydrogen storage, *RSC Adv.*, 2017, **7**, 27905–27912.

10 Y. Ding, C. Li, X. Zhang, W. Chen, X. Yu and G. Xia, Spatial confinement of lithium borohydride in bimetallic CoNi-doped hollow carbon frameworks for stable hydrogen storage, *ACS Appl. Mater. Interfaces*, 2024, **16**, 50717–50725.

11 S. Wang, M. Gao, Z. Yao, Y. Liu, M. Wu, Z. Li, Y. Liu, W. Sun and H. Pan, A nanoconfined-$LiBH_4$ system using a unique multifunctional porous scaffold of carbon wrapped ultrafine Fe_3O_4 skeleton for reversible hydrogen storage with high capacity, *Chem. Eng. J.*, 2022, **428**, 131056.

12 K. Xian, B. Nie, Z. Li, M. Gao, Z. Li, C. Shang, Y. Liu, Z. Guo and H. Pan, TiO2 decorated porous carbonaceous network structures offer confinement, catalysis and thermal conductivity for effective hydrogen storage of LiBH4, *Chem. Eng. J.*, 2021, **407**, 127156.

13 W. Chen, Y. Liu, C. Li, Y. Pang, X. Yu and G. Xia, Enhancing reversible hydrogen storage performance of $LiBH_4$ catalyzed by N-doped carbon nanosheet networks embedded with Co nanoparticles, *ACS Appl. Mater. Interfaces*, 2025, **17**, 50603–50611.

14 Y. Liu, W. Chen, S. Ju, X. Yu and G. Xia, Stable hydrogen storage of lithium borohydrides via the catalytic effect of Ni_2B induced by thermodynamic destabilization reaction, *J. Mater. Sci. Technol.*, 2024, **202**, 192–200.

15 Z. Z. Fang, X. D. Kang, P. Wang and H.-M. Cheng, Improved reversible dehydrogenation of $LiBH_4$ by milling with as-prepared single-walled nanotubes, *J. Phys. Chem. C*, 2008, **112**, 17023–17029.

16 G. Na, W. G. Cui, H. Shi, Z. Li, F. Gao, X. Wang, K. Wang, Y. Gao, Y. Yang, Z. Shen, Y. Liu, J. Miao and H. Pan, In situ generation and stabilization of multiple catalysts by introducing a graphene-supported FeF_2/FeO_x additive for enhancing the hydrogen storage of $LiBH_4$, *ACS Appl. Energy Mater.*, 2025, **8**, 3802–3811.

17 Y. Pang, X. Hu, X. Zhang, X. Yu and G. Xia, Two-dimensional transition metal-based high-entropy oxide nanoplates for enhanced hydrogen storage of $LiBH_4$, *J. Alloys Compd.*, 2025, **1040**, 183613.

18 X. Zhang, L. Zhang, W. Zhang, Z. Ren, Z. Huang, J. Hu, M. Gao, H. Pan and Y. Liu, Nano-synergy enables highly reversible storage of 9.2 wt% at mild conditions with lithium borohydride, *Nano Energy*, 2021, **83**, 105839.

19 J. J. Vajo, S. L. Skeith and F. Mertens, Reversible storage of hydrogen in destabilized $LiBH_4$, *J. Phys. Chem. B*, 2005, **109**, 3719–3722.

20 Q. He, D. Zhu, X. Wu, D. Dong, M. Xu and Z. Tong, Hydrogen desorption properties of $LiBH_4$/x$LiAlH_4$ (x = 0.5, 1, 2) composites, *Molecules*, 2019, **24**, 1861.

21 J. H. Shim, Y. S. Lee, J. Y. Suh, W. Cho, S. S. Han and Y. W. Cho, Thermodynamics of the dehydrogenation of the $LiBH_4$-YH_3 composite: Experimental and theoretical studies, *J. Alloys Compd.*, 2012, **510**, L9–L12.

22 N. Bergemann, C. Pistidda, M. Uptmoor, C. Milanese, A. Santoru, T. Emmler, J. Puszkiel, M. Dornheim and T. Klassen, A new mutually destabilized reactive hydride system: $LiBH_4$-Mg_2NiH_4, *J. Energy Chem.*, 2019, **34**, 240–254.

23 P. S. Miedema, P. Ngene, A. M. J. van der Eerden, D. Sokaras, T. C. Weng, D. Nordlund, Y. S. Au and F. M. F. de Groot, In-situ X-ray Raman spectroscopy study of hydrogen sorption properties of lithium borohydride composites, *Phys. Chem. Chem. Phys.*, 2014, **16**, 22651–22658.

24 X. Liu, E. H. Majzoub, V. Stavila, R. K. Bhakta, M. D. Allendorf, D. T. Shane, M. S. Conradi, N. Verdal, T. J. Udovic and S. J. Hwang, Probing the unusual anion mobility of $LiBH_4$ confined in highly ordered nanoporous carbon frameworks via solid state NMR and quasielastic neutron scattering, *J. Mater. Chem. A*, 2013, **1**, 9935–9941.

25 Y. Yan, H. Wang, M. Zhu, W. Cai, D. Rentsch and A. Remhof, Direct rehydrogenation of $LiBH_4$ from H-deficient $Li_2B_2H_{12-x}$, *Crystals*, 2018, **8**, 131.

26 P. Ngene, M. R. van Zwienen and P. E. de Jongh, Reversibility of the hydrogen desorption from $LiBH_4$: A synergetic effect of nanoconfinement and Ni addition, *Chem. Commun.*, 2010, **46**, 8201–8203.

27 F. Wang, J. Xu, X. Shao, X. Su, Y. Huang and T. Zhang, Palladium on nitrogen-doped mesoporous carbon: A bifunctional catalyst for formate-based, carbon-neutral hydrogen storage, *ChemSusChem*, 2016, **9**, 246–251.

28 K. Koh, M. Jeon, D. M. Chevrier, P. Zhang, C. W. Yoon and T. Asefa, Novel nanoporous N-doped carbon-supported ultrasmall Pd nanoparticles: Efficient catalyst for hydrogen storage and release, *Appl. Catal., B*, 2017, **203**, 820–828.

29 I. Muhammad, J. Saddique, C. Wu, M. ur Rahman, Z. U. Khan, W. Ali and R. Zhang, Nitrogen-doped -graphene-supported nickel nanoparticles reveal low dehydrogenation temperature and long cyclic life of magnesium hydrides, *ACS Omega*, 2024, **9**, 19261–19271.

30 X. Zhang, Y. Sun, S. Ju, J. Ye, X. Hu, W. Chen, L. Yao, G. Xia, F. Fang, D. Sun and X. Yu, Solar-driven reversible hydrogen storage, *Adv. Mater.*, 2023, **35**, 2206946.

31 X. Hu, X. Chen, X. Zhang, Y. Meng, G. Xia, X. Yu, D. Sun and F. Fang, In situ construction of interface with photothermal and mutual catalytic effect for efficient solar-driven reversible hydrogen storage of MgH_2, *Adv. Sci.*, 2024, **11**, 2400274.

32 X. Zhang, S. Ju, C. Li, J. Hao, Y. Sun, X. Hu, W. Chen, J. Chen, L. He, G. Xia, F. Fang, D. Sun and X. Yu, Atomic reconstruction for realizing stable solar-driven reversible hydrogen storage of magnesium hydride, *Nat. Commun.*, 2024, **15**, 2815.

33 Y. Jiang, Y. Sun, Y. Liu, M. Yue, Y. Cao, Q. Yuan and Y. Wang, Solar-driven reversible hydrogen storage in metal oxides-catalyzed MgH_2, *Int. J. Hydrogen Energy*, 2025, **149**, 150101.

34 Y. Sun, Y. Jiang, Y. Liu, L. Feng, M. Yue, Y. Cao and Y. Wang, Solar-driven rapid dehydrogenation of $LiBH_4$ catalyzed by g-C3N4/α-Fe_2O_3 heterojunction, *Int. J. Hydrogen Energy*, 2026, **200**, 152958.

35 H. Wang, Q. Li, J. Chen, J. Chen and H. Jia, Efficient solar-driven CO_2 methanation and hydrogen storage over nickel catalyst derived from metal-organic frameworks with rich oxygen vacancies, *Adv. Sci.*, 2023, **10**, 2304406.

36 K. Tan, Q. Pei, Y. Yu, L. Liu, J. Li, L. Han, Y. Yu, Z. Li, A. Munyentwali, J. Guo, Y. Wang, L. Rao, T. He and P. Chen, Solar-driven reversible hydrogen storage of sodium cyclohexanolate/phenoxide pair, *Angew. Chem., Int. Ed.*, 2025, **64**, e202506275.

37 S. S. Kim, A. Karkamkar, T. J. Pinnavaia, M. Kruk and M. Jaroniek, Synthesis and characterization of ordered, very large pore MSU-H silicas assembled from water-soluble silicates, *J. Phys. Chem. B*, 2001, **105**, 7663–7670.

38 S. S. Kim, T. R. Pauly and T. J. Pinnavaia, Non-ionic surfactant assembly of ordered, very large pore molecular sieve silicas from water soluble silicates, *ChemComm*, 2000, **17**, 1661–1662.

39 S. H. Joo, R. Ryoo, M. Kruk and M. Jaroniec, Evidence for general nature of pore interconnectivity in 2-dimensional hexagonal mesoporous silicas prepared using block copolymer templates, *J. Phys. Chem. B*, 2002, **106**, 4640–4646.

40 S. S. Kim and T. J. Pinnavaia, A low cost route to hexagonal mesostructured carbon molecular sieves, *ChemComm*, 2001, **23**, 2418–2419.

41 X. Liu, D. Peaslee, C. Z. Jost and E. H. Majzoub, Controlling the decomposition pathway of $LiBH_4$ via confinement in highly ordered nanoporous carbon, *J. Phys. Chem. C*, 2010, **114**, 14036–14041.

42 M. Oschatz, J. P. Hofmann, T. W. van Deelen, W. S. Lamme, N. A. Krans, E. J. M. Hensen and K. P. de Jong, Effects of the functionalization of the ordered mesoporous carbon support surface on iron catalysts for the Fischer-Tropsch synthesis of lower olefins, *ChemCatChem*, 2017, **9**, 620–628.

43 B. Lesiak, L. Kövér, J. Tóth, J. Zemek, P. Jiricek, A. Kromka and N. Rangam, C sp^2/sp^3 hybridisations in carbon nanomaterials – XPS and (X)AES study, *Appl. Surf. Sci.*, 2018, **452**, 223–231.

44 H. Darmstadt, C. Roy, S. Kaliaguine, S. J. Choi and R. Ryoo, Surface chemistry of ordered mesoporous carbons, *Carbon*, 2002, **40**, 2673–2683.

45 L. M. Chew, W. Xia, H. Düdder, P. Weide, H. Ruland and M. Muhler, On the role of the stability of functional groups in multi-walled carbon nanotubes applied as support in iron-based high-temperature Fischer–Tropsch synthesis, *Catal. Today*, 2016, **270**, 85–92.

46 Y. J. Cho, S. Y. Kang, B. C. Wood and E. S. Cho, Heteroatom-doped graphenes as actively interacting 2D encapsulation media for Mg based hydrogen storage, *ACS Appl. Mater. Interfaces*, 2022, **14**, 20823–20834.

47 Q. Wang, J. Su, H. Chen, D. Wang, X. Tian, Y. Zhang, X. Feng, S. Wang, J. Li and H. Jin, Highly conductive nitrogen-doped sp^2/sp^3 hybrid carbon as a conductor-free charge storage host, *Adv. Funct. Mater.*, 2022, **32**, 2209201.

48 S. D. S. Fitch, G. E. Moehl, N. Meddings, S. Fop, S. Solue, T. L. Lee, M. Kazemian, N. G. Araez and A. L. Hector, Combined electrochemical, XPS, and STXM study of lithium nitride as a protective coating for lithium metal and lithium-sulfur batteries, *ACS Appl. Mater. Interfaces*, 2023, **15**, 39198–39210.

49 W. Hou, Y. Li, S. Li, Z. Liu, P. G. Ryan, M. Xu, J. K. Kim, B. Yuan, R. Hu and Z. Luo, Lithium dendrite suppression with Li_3N-rich protection layer formation on 3D anode via ultra-low temperature nitriding, *Chem. Eng. J.*, 2022, **441**, 136067.

50 S. Emani, C. Liu, M. Ashuri, K. Sahni, J. Wu, W. Yang, K. Nemeth and L. L. Shaw, Li_3BN_2 as a transition metal free, high capacity cathode for Li-ion batteries, *ChemElectroChem*, 2019, **6**, 320–325.

51 Y. Pang, C. Wei, X. Ye, X. Li, H. Sun, S. Luo, T. Chen, S. Xia, T. Yuan and S. Zheng, $H^{\delta-}$–$H^{\delta+}$ comproportionation enables stable Li-N-H-F solid electrolyte, *Angew. Chem., Int. Ed.*, 2025, **64**, e202511344.

52 J. Legrand, A. Taleb, S. Gota, M. J. Guittet and C. Petit, Synthesis and XPS characterization of nickel boride nanoparticles, *Langmuir*, 2002, **18**, 4131–4137.

53 J. Hong, M. Miola, D. Gerlach, M. C. A. Stuart, P. Rudolf, D. M. Morales, L. Protesescu and P. P. Pescarmona, An exploration of the electrocatalytic activity of nickel boride nanocrystals in the oxidation of 5-HMF, *Catal. Sci. Technol.*, 2025, **15**, 457–475.

54 H. E. Kissinger, Variation of peak temperature with heating rate in differential thermal analysis, *J. Res. Natl. Bur. Stand.*, 1956, **57**, 217–221.

55 J. L. White, A. A. Baker, M. A. Marcus, J. L. Snider, T. C. Wang, J. R. I. Lee, D. A. L. Kilcoyne, M. D. Allendorf, V. Stavila and F. El Gabaly, The inside-outs of metal hydride dehydrogenation: imaging the phase evolution of the Li-N-H hydrogen storage system, *Adv. Mater. Interfaces*, 2020, **7**, 1901905.

56 Y. E. Filinchuk, K. Yvon, G. P. Meisner, F. E. Pinkerton and M. P. Balogh, On the composition and crystal structure of the new quaternary hydride phase $Li_4BN_3H_{10}$, *Inorg. Chem.*, 2006, **45**, 1433–1435.

57 D. J. Siegel, C. Wolverton and V. Ozoliņs, Reaction energetics and crystal structure of $Li_4BN_3H_{10}$ from first principles, *Phys. Rev. B: Condens. Matter Mater. Phys.*, 2007, **75**, 014101.

58 J. F. Herbst and L. G. Hector, Jr, Electronic structure and energetics of the quaternary hydride $Li_4BN_3H_{10}$, *Appl. Phys. Lett.*, 2006, **88**, 231904.

59 P. Ngene, M. H. W. Verkuijlen, Q. Zheng, J. Kragten, P. J. M. van Bentum, J. H. Bitter and P. E. de Jongh, The role of Ni in increasing the reversibility of the hydrogen release from nanoconfined $LiBH_4$, *Faraday Discuss.*, 2011, **151**, 47–58.

